On the application of artificial neural network for the development of a nonlinear aeroelastic model

A.J. Torregrosa, L.M. García-Cuevas, P. Quintero, A. Cremades *

CMT-Motores Térmicos, Universitat Politècnica de València, Camino de Vera s/n, Valencia, 46022, Spain

A R T I C L E I N F O	A B S T R A C T

Aeroelastic Computational Fluid Dynamics simulations have traditionally been associated to a high computational cost, making them prohibitive in a initial phase of the design. Analytic models, which may not be accurate for nonlinear aerodynamics, have traditionally been utilized in order to size those structures. Recently, some authors have proposed the use of artificial neural networks to reduce the error in the prediction of aerodynamic coefficients of bluff bodies, which have separated flow over a substantial part of its wetted surface. This article proposes a method based on neural networks for calculating the dynamic aerodynamic coefficients of a flat plate. The procedure, which is applied for different network typologies (feed-forward and long-short term memory neural networks), is, then, coupled with a structural solver in order to create an aeroelastic reduced order model. The results are compared with CFD aeroelastic simulations, showing a high reduction of computational cost (99%) without penalties in the accuracy. The instabilities are captured and the mean deformation, amplitude and frequency of the motion are predicted. In addition, the different neural network models are compared evidencing that for the aeroelastic calculation feed-forward networks are most efficient in terms of accuracy and computational cost.

1. Introduction

Modern structures are designed to reduce the amount of material required to prevent failure. As the frame weight is decreased, the structure becomes more efficient and environmentally sustainable. Moreover, saving resources supposes a reduction on its cost of production, obtaining a more competitive product [1]. However, the improvement on the weight is also related with a decrease of the torsion and bending stiffness of the frame, evidencing the necessity of finding a Pareto-optimal solution of structural integrity and cost. For applications where the structure is exposed to wind loads, the reduction of stiffness may increase the effect of the aeroelastic phenomena, producing instabilities at low free stream velocities [2].

Due to the previous reasons, aeroelastic analysis has been a hot topic in aerospace [3], civil [4] or automotive [5] engineering, and a wide amount of literature dealing with these phenomena can be found. Some researchers analyzed divergence experimentally [6], analytically [7] or numerically [8]. Other authors focused on other effects as flutter [9], [10] or buffeting [11], [12].

The study of the aeroelastic problem may be carried out using different tools and approaches. A research might be conducted analytically [13], numerically [14] or experimentally [15]. Among the latest, the studies may be performed directly on a manufactured product or using a wind tunnel model. Relative to the first option, Evans et al. [16] carried out measurements of the deformation of a 5 kW wind turbine. Argentini et al. [17] used a wind tunnel model to analyze the buffeting response of long span bridges. Although wind tunnels are useful to reproduce the wind flow under controlled conditions, these experiments have many restrictions as the scale effects, wall and support interference and aerodynamic distortion [18]. These limitations evidence the importance of using other methods, such as Computational Fluid Dynamics (CFD) simulations, to verify the results.

Additionally, numerical simulations may also be used to calculate aeroelastic phenomena. In order to calculate the whole set of equations, a CFD / Computational Solid Dynamics (CSD) analysis could be performed. For instance, Dong et al. [19] and Ren et al. [20] predicted flutter in turbomachinery and Wang et al. [21] calculated a 3D wind turbine blade. Nevertheless, the computational cost associated with the resolution of the complete set of equations is unaffordable for most engineering problems and, therefore, many authors as Peng and Jinglong [22], Tsushima and Su [23], Amoozgar et al. [24] and Kwon et al. [25] reduced the

Nomenclature

Symbols

α	Angle of attack
$\triangle \alpha$	Angle of attack amplitude of the motion
$\triangle \theta$	Pitch amplitude of the motion
$\triangle t$	Time step
$\triangle x$	Cell size
$\triangle w$	Plunge amplitude of the motion
ϵE_{c_m}	Energetic error of the oscillation cycle
Θ	Amplitude of the forced oscillations
θ	Pitch of the section
θ^*	Nondimensional pitch of the section
θ_0	Initial pitch of the section
$\bar{\theta}$	Mean pitch of the section
μ_∞	Free stream viscosity
ρ_∞	Free stream density
$\mathbf{A}$	Matrix of the linear system
a_∞	Free stream sound speed
$\vec{b}$	Vector of the linear system
c	Chord of the plate
c_m	Moment coefficient
c_m^{dyn}	Dynamic moment coefficient
c_m^{st}	Steady moment coefficient
c_l	Lift coefficient
c_{l0}	Zero angle of attack lift coefficient
$c_{l\alpha}$	Lift coefficient angle of attack derivative
$c_{l\dot{\alpha}}$	Lift coefficient angle of attack velocity derivative

$c_{l\ddot{\alpha}}$	Lift coefficient angle of attack acceleration derivative
c_l^{dyn}	Dynamic lift coefficient
c_l^{st}	Steady lift coefficient
c_p	Power coefficient
f	Frequency of the motion
f_1, f_2, f_3, f_4	Intermediate steps in 4th order Runge-Kutta
H	Width of the channel
h	Thickness of the plate
I^*	Nondimensional inertia of the 2D section
I_{2D}	Inertia of the 2D section
k^*	Nondimensional stiffness
k_θ	Torsion stiffness
k_w	Bending stiffness
k_w^*	Nondimensional bending stiffness
L_u	Upstream length of the domain
L_d	Downstream length of the domain
m^*	Nondimensional mass of the 2D section
m_{2D}	Mass of the 2D section
Ma	Mach number
Re	Reynolds number
T	Period of the oscillation
t	Time
V_∞	Free stream velocity
w	Plunge of the section
$\bar{w}$	Mean plunge of the section
y^+	Nondimensional wall distance

complexity of the problem by using Euler equations, 2D unsteady potential model and modified small disturbance theory, respectively, for the calculation of the aerodynamic loads. Other researchers, as You et al. [26] have simplified the structure to a 1D beam reducing the cost of the computation of the CSD solver.

In order to reduce the computational cost associated with the 3D aeroelastic problem, many researchers calculate a characteristic aeroelastic section [27], which has been traditionally used in literature [28]. For instance, in the work of Camilo et al. [29], the aeroelastic response of a 2D section using CFD is analyzed to obtain the response of nonlinear structures. Even though, the cost of computing a wide range of unsteady 2D simulations is still high.

In order to reduce computing time, different Reduced Order Models (ROM) have been proposed [30]. A great amount of the aerodynamic ROMs are based on proper orthogonal decomposition (POD). Although these methods proved to be an accurate model in many problems, as the optimization of a compressor [31] or the aeroelastic calculation of a wing [32], POD "ROMs are only suitable for a frozen aeroelastic model configuration" [30]. The associated frequencies of the ROM are dependent upon the mass and stiffness distribution and, therefore, a change on the structure will lead to a different motion and eigenvalues of the flow field and, thus, to a different POD.

On the other hand, artificial neural networks (ANN) have demonstrated to be capable of predicting a wide range of physical phenomena, as compressor performance [33], volumetric efficiency of ICE [34] or diesel engine emissions [35]. Moreover, some authors have applied ANN to solve aerodynamic [36] and aeroelastic problems. For instance, Wu and Kareem [37] modeled the hysteretic nonlinear behavior of bridge decks under aerodynamic load. In their paper, the aerodynamic coefficient is splitted into static and dynamic coefficients in order to obtain the nonlinearities in a turbulent flow. Another example is the research of Chen et al. [38], in which the flutter derivatives of a flat plate are calculated using an artificial neural network fed with experimental data. In other

papers, as Abbas et al. [39] and Li et al. [40], the artificial neural network is fitted using CFD results. In Abbas et al. [39] the network is joined with a structural solver in order to obtain the aeroelastic response. However, the aerodynamic model only uses feed forward networks (FFN) and, thus, the capabilities of deep learning tools such as Long Short Term Memory (LSTM) networks are not evaluated. Furthermore, in Li et al. [40], an LSTM network is used to calculate the unsteady aerodynamic behavior of a bridge deck. Nevertheless, the author does not compare the LSTM solutions with FFN, evaluating the convenience, precision and limitations of each typology.

This paper aims at completing the research developed in the literature, proposing a reduced order model (ROM) for decreasing computing time in the initial design of beams under wind loads. The ROM will be applied to a 2D flat plate geometry immersed in a wind channel. The flat plate is chosen because it experiences nonlinear aerodynamic phenomena even for low values of the angle of attack. In addition, the channel width is taken in a way such that the aerodynamics of the system will be influenced by the vertical position of the plate. Two different surrogate models, using FFN and LSTM networks are developed to estimate the aerodynamic loads. These models are fed by means of CFD calculations, and they are able to provide an accurate estimation of the nonlinear unsteady aerodynamic forces acting over the plate. The ANNs are coupled with a structural model, allowing the estimation of the nonlinear aeroelastic features with a relatively low computational cost.

The paper is structured as follows. First, in Section 2, the main geometrical features of the test case will be described. Later, in Section 3, a full description of the theoretical bases of the problem are provided. After that, in Section 4, the ANN and CFD methodologies will be explained in order to obtain the main results, which will be collected later, at Section 5. Finally, the main conclusions of the work will be provided, at Section 6.
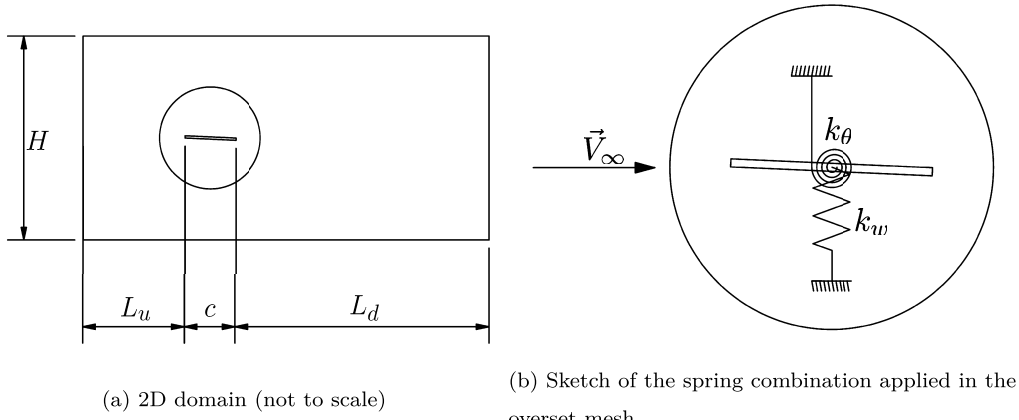
(a) 2D domain (not to scale)

(b) Sketch of the spring combination applied in the overset mesh.

Fig. 1. Domain of the simulation (not to scale), 3D plate simulation (left) and 2D simplification of the problem (right).

2. Description of the test case

The test case consists of a flat plate immersed in a wind tunnel, taken from Gil et al. [41], as shown in Fig. 1. The structure is reduced to a combination of linear and torsional springs, Fig. 1b. The flat plate section is selected due to its aerodynamic nonlinearities for low angles of attack, as well as its similarities to important engineering elements such as solar panels. The channel is also included in the analysis to take into account the effect of the vertical position in the aerodynamic steady coefficients. The plate has a chord $c = 0.1$ m, and a thickness $h = 0.04c$. The channel presents the following dimensions: upstream length $L_u = 5c$, downstream length $L_d = 15c$ and a width of $H = 4c$, Fig. 1a. Upstream and downstream dimensions are taken in a manner that the inlet and outlet boundary conditions do not affect the simulation.

The walls of the channel are supposed sufficiently far from the plate for assuming slip boundary conditions (Euler walls) without affecting substantially the aerodynamic response of the flat plate, similarly as in [42]. The inlet flow is perpendicular to the inlet section. The characteristics of the flow are: density $\rho_\infty = 1.18$ kg/m³, viscosity $\mu_\infty = 1.85 \cdot 10^{-5}$ Pa s and a sound speed of $a_\infty = 340$ m/s. The velocity V_∞ is varied between 7 m/s and 42 m/s. Thus, Reynolds number (Re $= \frac{\rho_\infty V_\infty c}{\mu_\infty}$) changes between $4.5 \cdot 10^4$ and $2.7 \cdot 10^5$; and Mach number (Ma $= \frac{V_\infty}{a_\infty}$) between 0.02 and 0.12. The holding structure of the plate is reproduced by means of two springs of torsional and linear stiffness $k_\theta = 30.46$ Nm/m and $k_w = 558.46$ N/m² respectively, Fig. 1b. Finally, the mass and inertia of the section are $m_{2D} = 0.36$ kg/m and $I_{2D} = 3.9 \cdot 10^{-4}$ kgm²/m.
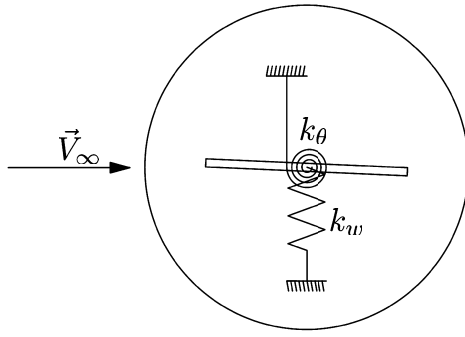
3. Theoretical background

In this section, the main aeroelastic equations are introduced. In addition, the basis of artificial neural network is exposed, showing the principal typologies used in this work. Finally, the CFD models are presented.

3.1. Aeroelastic equivalent section

The motion of the equivalent 2D section is governed by Equations (1) and (2), which states the equilibrium for torsional and vertical degrees of freedom respectively.

$$I_{2D}\ddot{\theta} + k_\theta \theta = \tfrac{1}{2}\rho_\infty c^2 V_\infty^2 \left(c_m^{st}(\alpha, w) + c_m^{dyn}(\bar{\alpha}, \Delta\alpha, \dot{\alpha}, \ddot{\alpha}) \right) \rightarrow$$
$$I^*\ddot{\theta}^* + k^*\theta^* = c_m^{st}(\alpha, w) + c_m^{dyn}(\bar{\alpha}, \Delta\alpha, \dot{\alpha}, \ddot{\alpha})$$

(1)

$$m_{2D}\ddot{w} + k_w w = \tfrac{1}{2}\rho_\infty c V_\infty^2 \left(c_l^{st}(\alpha, w) + c_l^{dyn}(\bar{\alpha}, \Delta\alpha, \dot{\alpha}, \ddot{\alpha}) \right) \rightarrow$$
$$m^*\ddot{w}^* + k_w^* w^* = c_l^{st}(\alpha, w) + c_l^{dyn}(\bar{\alpha}, \Delta\alpha, \dot{\alpha}, \ddot{\alpha})$$

(2)

where the angle of torsion of the plate is θ, the aerodynamic angle of attack is α, w is the plunge and θ^* and w^* are the nondimensional torsion and plunge. The nondimensional numbers governing the behavior of the plate (the nondimensional torsional stiffness, Equation (3), the nondimensional inertia, Equation (4), the nondimensional flexural stiffness, Equation (5) and the nondimensional mass, Equation (6)) may be calculated in order to reproduce a three-dimensional structure, as demonstrated by Gil et al. [41]:

$$k^* = \frac{k_\theta}{\tfrac{1}{2}\rho_\infty v_\infty^2 c^2}$$

(3)

$$I^* = \frac{I_{2D}}{\tfrac{1}{2}\rho_\infty c^4}$$

(4)

$$k_w^* = \frac{k_w}{\tfrac{1}{2}\rho_\infty v_\infty^2 c}$$

(5)

$$m^* = \frac{m_{2D}}{\tfrac{1}{2}\rho_\infty c^2}$$

(6)

Following as Wu and Kareem [37], the aerodynamic coefficients (c_l and c_m) of equations (1) and (2) are expressed as the sum of the stationary, c_l^{st} and c_m^{st}, and the dynamic terms, c_l^{dyn} and c_m^{dyn}. In addition, $\bar{\alpha}$ is the average value of the angle of attack of the oscillation and $\Delta\alpha$ is the increment of angle of attack with respect to $\bar{\alpha}$. The angle of attack might be defined as a function of the motion variables θ and w:

$$\alpha = \theta - \arctan\left(\frac{\dot{w}}{V_\infty}\right) \approx \theta - \frac{\dot{w}}{V_\infty}$$

(7)

3.2. Artificial neural networks

ANN are routinely used for regression problems, easily approximating any continuous function. In this work, ANN are trained with data from the aerodynamic simulations, leading to improvements in the estimations of the aerodynamic performance of the plate over those of the stationary and linear aerodynamic models. The networks have been calculated by using TensorFlow with Keras engine. In this paper, two different models have been tested and compared for predicting the nonlinear aerodynamic coefficients of a flat plate: Feed Forward Networks and a Long Short Term Memory networks. FFN obtain the value of the coefficients using the input variables of the calculated time step. On the other
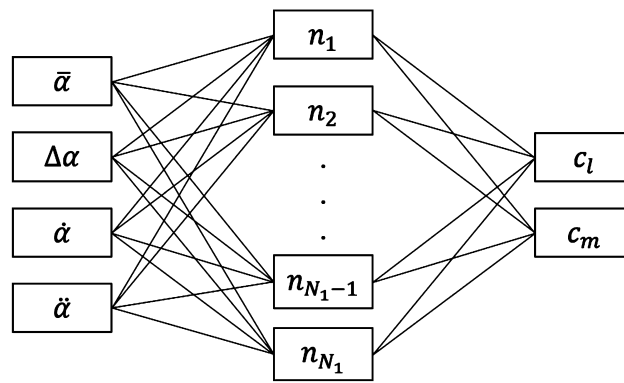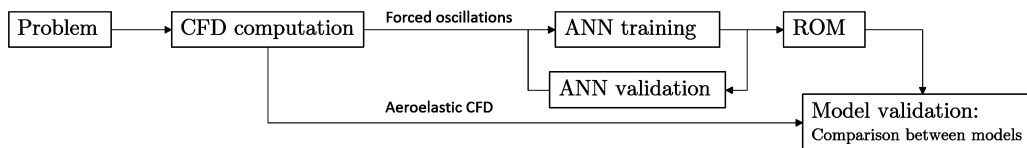
Fig. 2. Schematic architecture of the ANN.

Fig. 3. Scheme of the work flow of the aeroelastic ROM. The procedure includes training, validation and application of the ANN.

hand, LSTM networks accumulate the information of all the previous time steps [43]. Both types of networks have been tested with the same architecture, Fig. 2. All the studied networks use a multi layer perceptron with three layers: input layer, hidden layer and output layer. The number of neurons of the hidden layer, N_1, is optimized in terms of computational cost and accuracy, as explained in Section 4. In addition, as the aerodynamic coefficients are continuous, the activation functions of the neurons must also be continuous.

In order to use ANN, the network must be trained using data, which can be obtained from different sources. In this work, a virtual CFD wind tunnel has been used to generate the information of the training data. However, the method admits data obtained from different sources. The training process has been performed for both types of network using a RMSprop algorithm, until training and test loss function reach an asymptotic behavior or start to increase, to prevent from overfitting.

3.3. Computational fluid dynamics

The aerodynamic forces acting on the test case can be obtained using different tools and approaches. One of these tools is CFD, which calculates the solution of the conservation equations of the fluid. Here, the simulations, which have been calculated using commercial software Simcenter STAR-CCM+®, make use of the Unsteady Reynolds-averaged Navier-Stokes equations [44]. A $k - \omega$ with shear stress transport (SST) turbulence model is utilized because it has been proved to predict accurate results under adverse pressure gradient as the ones appearing in a flat plate ([45] and [46]). The $k - \omega$ SST was proposed by Wilcox [47] to solve the limitations of the $k - \omega$ far from the walls, where a $k - \epsilon$ model is used. This model requires to maintain the value of the nondimensional wall distance to the first layer of computational cells, y^+, in the viscous sublayer ($y^+ < 5$) for the major part of the wall.

4. Methodology

Along this section the methodology for the different submodels and calculation is presented. First, the CFD data base construction is detailed: the oscillations are defined and CFD mesh and setup preparation is explained. Then the Artificial Neural Network model

training and validation is presented. The optimum number of neurons is calculated, the data set error is analyzed and the results of the training and test of the network are shown. Finally, the coupled solver algorithm is described and the numerical models are described. The complete methodology of the paper is summarized in the diagram of Fig. 3.

4.1. CFD: data base construction

The training data set is constructed with a matrix of 324 CFD bidimensional forced oscillation simulations, which are selected to be representative of a wide range of physical conditions. In addition, the initial angle of attack and the amplitude of the movement is limited to the range in which vortex shedding is negligible, which is similar to many engineering problems, as solar panels in stow position [48]. Strong vortex shedding leads to important random oscillations of the aerodynamic coefficients, decreasing the accuracy of the network under interest conditions. Finally, the fluid-structure interaction is calculated through a strongly coupled algorithm, which shows stability under strong nonlinear interactions [49].

The training simulations represent a forced oscillatory pitching motion with the formulation of equation (8):

$$\theta = \theta_0 + \Theta \sin(2\pi f t) \tag{8}$$

being θ_0 the initial pitch angle, Θ the amplitude of the motion and f the frequency of the motion. The matrix of simulations contains the training cases shown in Fig. 4.

The simulation is performed using the commercial software Simcenter STAR-CCM+® over the domain of Fig. 1a. The discretization of the domain is made with a polygonal mesh, as presented in Fig. 6. A coupled solver with second order upwind ROE FDS scheme is used for computing the advection terms ([50], [51]), whereas the gradients are computed with a hybrid Gauss-Least Squares Method with Venkatakrishnan limiter [52]. The rotation is established using an overset region in the near field [53]. A mesh of $5.1 \cdot 10^4$ elements has been chosen making a mesh independence process based on Richardson's extrapolation (RE) [54]. A spatial discretization error lower than the 2% has been obtained for the major part of the aerodynamic domain. The value of the
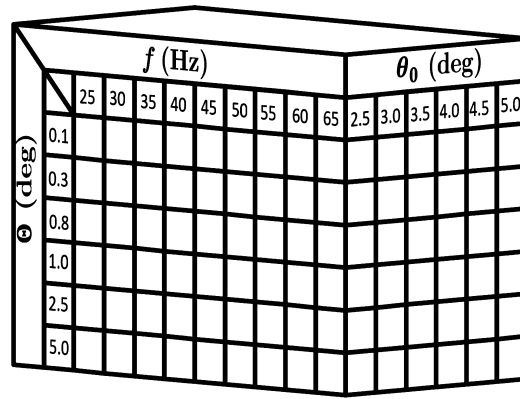
Fig. 4. Training simulation data set matrix.

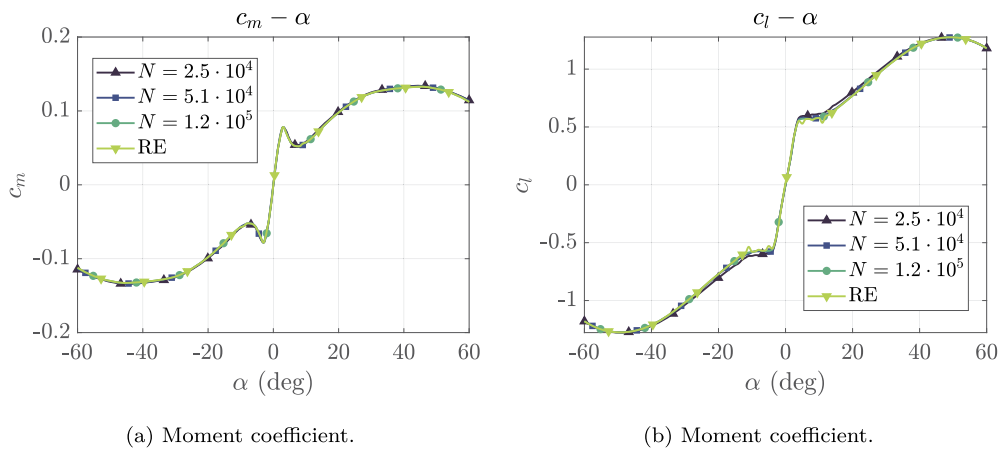
(a) Moment coefficient.

(b) Moment coefficient.

Fig. 5. Computation of aerodynamic lift and moment coefficient for different meshes. Comparison with RE. N is the number of elements of the mesh.
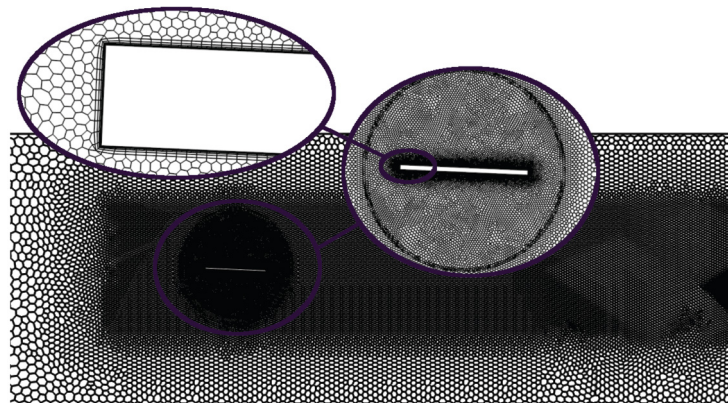

Fig. 6. Sketch of the computational mesh (not to scale) showing the different zones of refinement.

aerodynamic coefficients obtained using these methods can be observed in Fig. 5. The final mesh has a size of $\Delta x_{\text{global}} = 0.02$ m, $\Delta x_{\text{wake}} = 0.004$ m in the wake, $\Delta x_{\text{overset}} = 0.002$ m in the overset and $\Delta x_{\text{wall}} = 0.0004$ m. Some details of the computational mesh can be seen in Fig. 6.

Relative to the time discretization, a second order scheme is utilized. The time step is selected to keep Courant-Friedrichs-Levy number ($CFL = \frac{\Delta t V}{\Delta x}$) below 1, as observed in Fig. 7, in order to obtain enough time resolution, similarly to Torregrosa et al. [42] and Adeniyi et al. [55]. To reach the previous CFL, the simulation uses a nondimesional time step of $\frac{t V_\infty}{c} = 0.002$ for the forced os-

cillations and between $7 \cdot 10^{-4}$ and 0.0042 in the aeroelastic cases. In Fig. 7b, the distribution of the nondimensional wall distance y^+ over the plate can be observed. Note that its value is lower than 5 in the whole wall, ensuring that the boundary layer remains in the viscous sublayer.

4.2. Artificial neural network: training and validation

In this section, the procedure to fit the phenomena of Section 4.1 with a neural network is presented. The influence of the number of neurons is analyzed, evaluating the energetic global error of the cycles, in Section 4.2.1. In addition, the training and val-
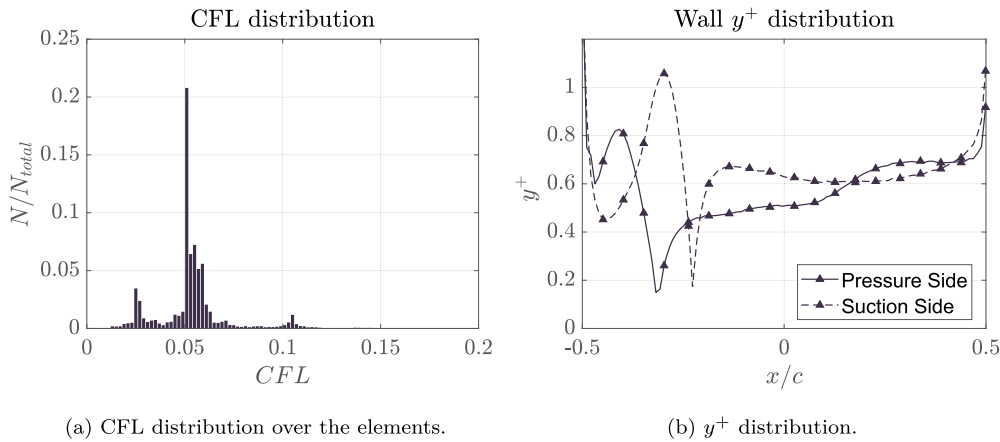
(a) CFL distribution over the elements.

(b) y^+ distribution.

Fig. 7. CFL distribution and nondimensional wall distance over the plate.

(a) 2 neurons in the hidden layer
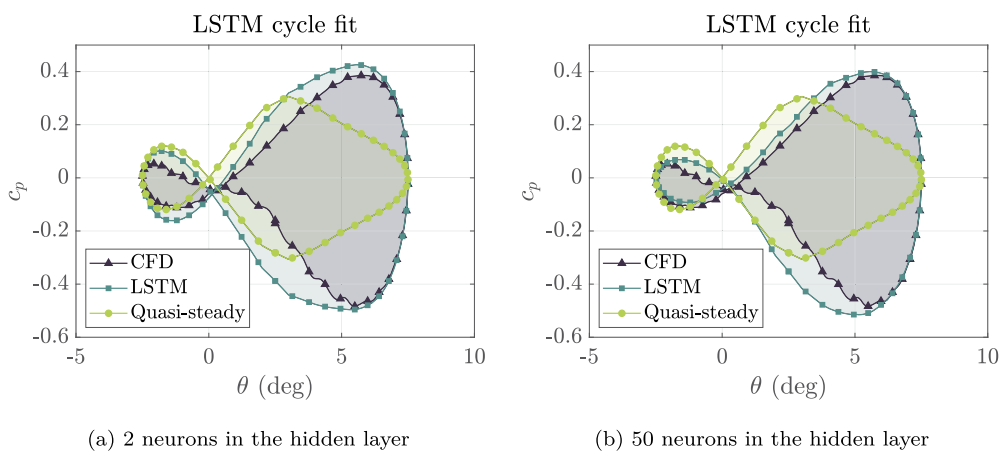
(b) 50 neurons in the hidden layer

Fig. 8. Power coefficient comparison between the ANNs and the CFD simulations for two representative number of neurons on the hidden layer. The cycle is shown for an initial incidence of 2.5 deg, an amplitude of 5 deg and a nondimensional frequency of $\frac{fc}{V_\infty} = 0.1250$.

idation mean squared errors are evaluated and analyzed in order to define the number of epochs required for the training process. All the studied networks have been trained using a RMSprop algorithm on 90% of the forced oscillation data. The remaining 10% which corresponds to arbitrary movements is used for the validation.

As stated in Section 3, the dynamic coefficient calculated by means of the neural networks is added to a stationary aerodynamic coefficient, called quasi-steady model. This quasi-steady model interpolates, linearly, the coefficients from the steady CFD results, as shown in Section 5. Therefore, the models shown in the section are: CFD (2D forced oscillations), quasi-steady (aerodynamic coefficients interpolated from steady polar), FNN and LSTM (dynamic coefficient calculated by means of FNN and LSTM respectively, added to the quasi-steady coefficient).

4.2.1. Neuron independence analysis

The number of neurons used to calculate the aerodynamic model states the number of weights and variables to adjust the ANN. Therefore, it determines the accuracy and computing cost of training the network [43], but also the probability of network overfitting. A neuron independence analysis is performed to reduce the number of neurons without affecting the results. This analysis is applied over the different configurations: FFN and LSTM. All the studied ANN consist of an input layer, a hidden layer with N_1 neurons and an output layer with $N_2 = 2$ neurons, as previously presented in Fig. 2.

To perform the neuron independence analysis, the energetic error of the aerodynamic cycle, ϵE_{c_m}, is calculated as the difference of power coefficients ($c_p = c_m \frac{\dot{\theta} c}{V_\infty}$) integrated in time for CFD and ANN, as stated by Equation (9).

$$\epsilon E_{c_m} = \frac{\int_t^{t+T} (c_{p_{ANN}}) dt - \int_t^{t+T} (c_{p_{CFD}}) dt}{\int_t^{t+T} (c_{p_{CFD}}) dt} \tag{9}$$

In Fig. 8, the power coefficient comparison between CFD and ANN is presented for a network of 2 and 50 neurons (Figs. 8a and 8b respectively). In the figure, an improvement of accuracy compared with the steady solution is observed.

In Fig. 9, the cycle energetic error density function is shown as a function of the number of neurons of the first layer for a FNN, Fig. 9a, and a LSTM network, Fig. 9b. Observe how for $N_1 = 50$, the energetic error becomes approximately constant, being 50 neurons the optimal choice in terms of accuracy and computational cost.

In addition, the error of the network also depends on the number of epochs of the training process [56]. The number of training epochs is selected to ensure that the logarithmic validation error has either reached an asymptotic limit or started to increase. Fig. 10 shows how the validation mean squared error (MSE) flattens for the previous number of epochs. In addition, a k-fold cross validation analysis [57] is performed, obtaining a mean prediction error of $5.34 \cdot 10^{-4}$ for 10-folds using the FNN model.

The distribution of the error in the whole data set is shown in Fig. 11. This figure shows the distribution of the input variables,
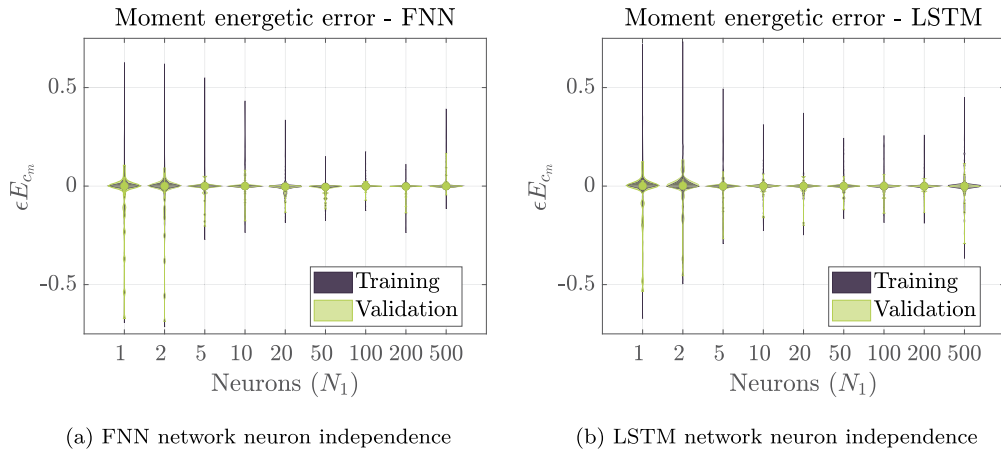
(a) FNN network neuron independence   (b) LSTM network neuron independence

Fig. 9. Distribution of the energy error for the different number of neurons. (For interpretation of the colors in the figure(s), the reader is referred to the web version of this article.)
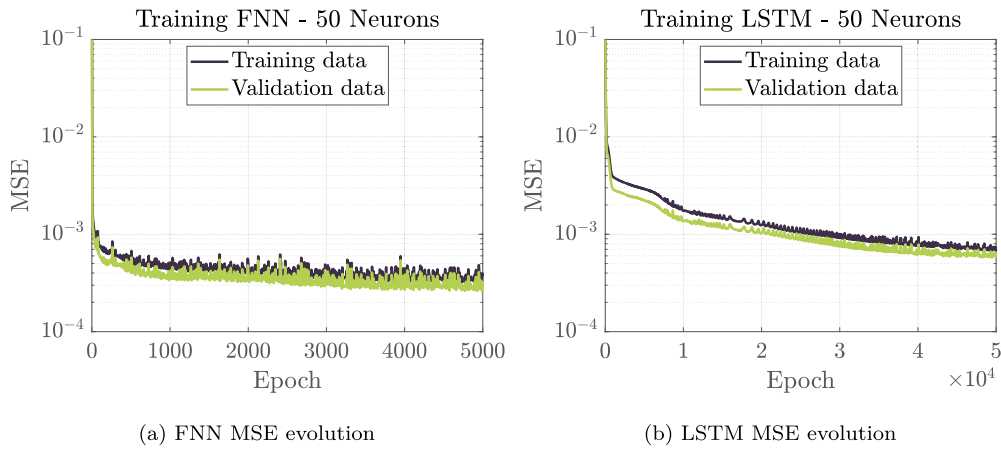

(a) FNN MSE evolution   (b) LSTM MSE evolution

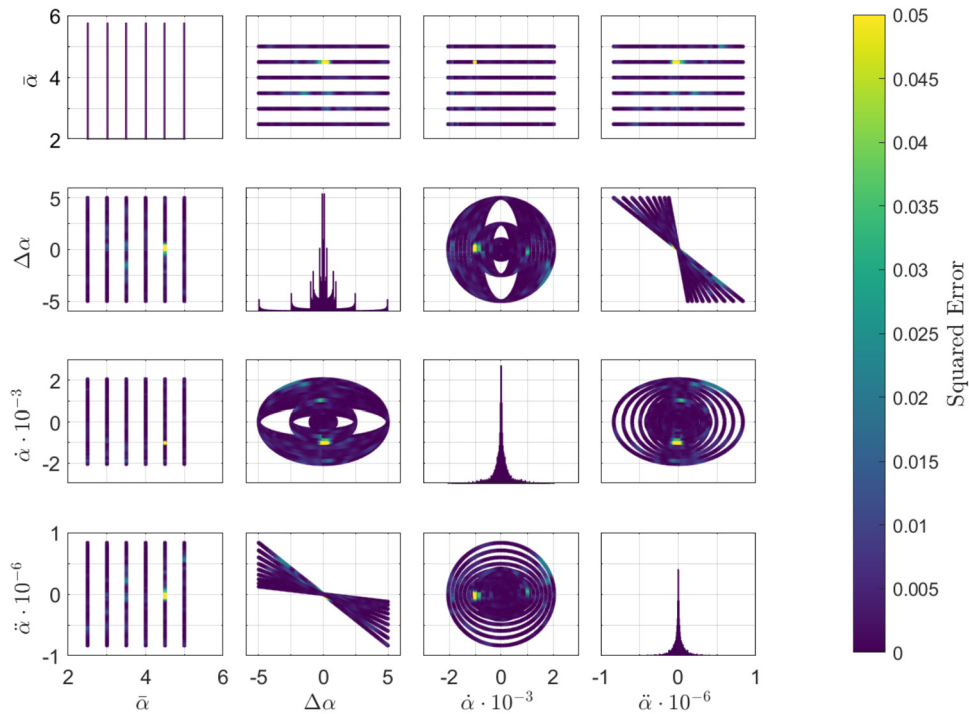**Fig. 10.** Evolution of the MSE as a function of the epoch of training for FNN and LSTM networks.

Fig. 11. Squared error distribution for the input variables. The plots on the diagonal show the distribution of the training variables, while the subfigures out of the diagonal show the squared error distribution for each pair of input variables.
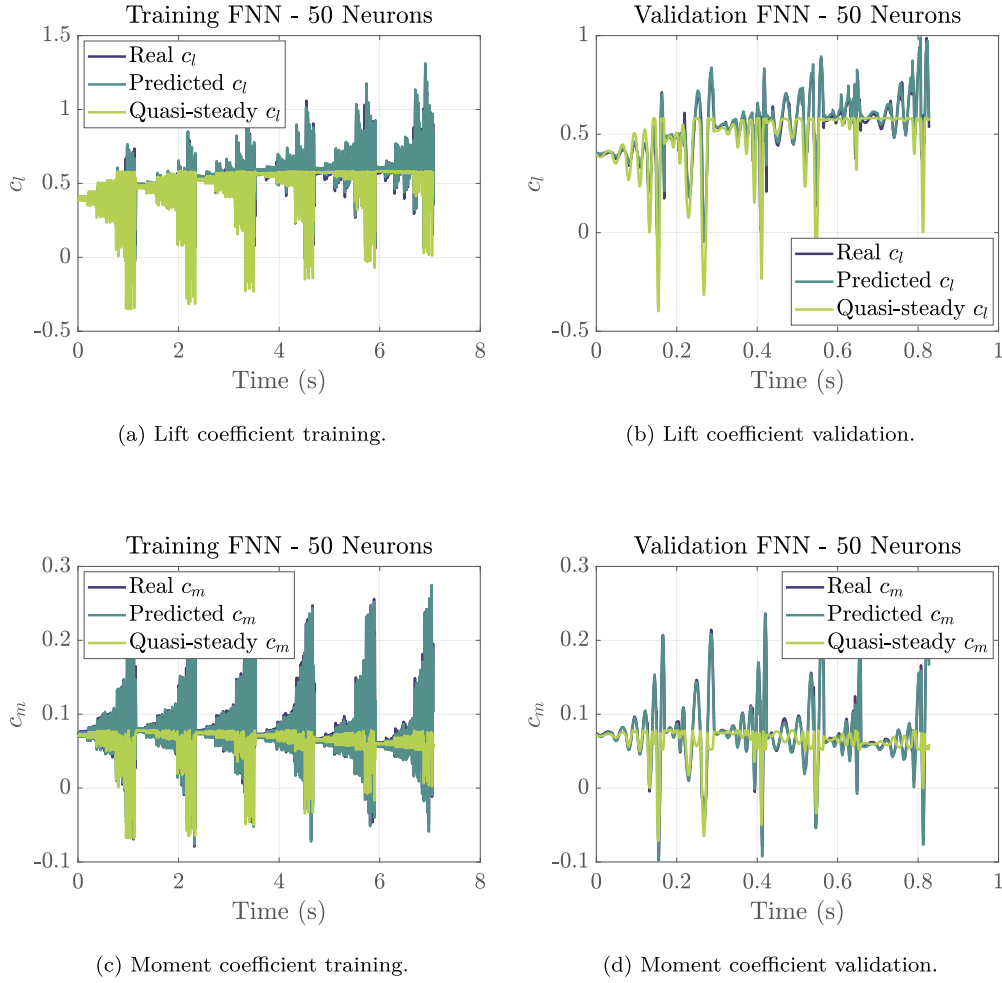
(a) Lift coefficient training.

(b) Lift coefficient validation.

(c) Moment coefficient training.

(d) Moment coefficient validation.

Fig. 12. Training and validation of the FNN neural network.

the points where the neural network has been evaluated and the areas with the higher error. The squared error is demonstrated to be low for the analysis domain, presenting the higher errors for the mean points of the oscillation near the stall point of the plate: incidence of 4.5 deg and null increment of the angle of attack.

In Figs. 12 and 13 the performance of the ANN is shown for training and validation data. Both typologies of networks show an accurate behavior in the simulation of nonlinear aerodynamics compared with the quasi-steady approach. Real and predicted values overlap in the major part of the cycles. Although the large amount of data makes it difficult to visualize the training curves, Fig. 14 evidences similar behavior in training and testing.

In order to clarify the results shown in Figs. 12 and 13, Fig. 14 shows the linear regression between the real and the predicted value of the coefficient, comparing it with the ideal non-error solution. A fair agreement between ANN predictions and CFD calculations can be observed in this Figure.

4.3. Aeroelastic ROM algorithm

The artificial neural network is coupled with a structural solver, Equations (1) and (2). The solution of the equations is integrated from the initial conditions using a four-step predictor-corrector algorithm. The ROM algorithm is illustrated in Fig. 15.

The model starts setting the initial conditions. A fourth order Runge-Kutta scheme is applied for the initialization due to its accurate results [58]. Finally, a four-step predictor-corrector is

utilized to integrate the differential equations. For a deeper explanation of the numerical methods, the reader is referred to Sections 4.3.1, 4.3.2 and 4.3.3. The aerodynamic forces are updated each time step, the steady coefficients are calculated by a 2D interpolation function and the dynamic coefficients are obtained by using an artificial neural network.

4.3.1. Aeroelastic equations: state system

The aeroelastic equations are linearly solved updating the aerodynamic forces and moments every time step. The aeroelastic linear system can be expressed in terms of the matrix A and the vector $\vec{b}$. The vectors $\vec{x}_t$ and $\dot{\vec{x}}_t$ represent the states of the system and its derivatives in the time step t respectively.

$$\dot{\vec{x}}_t = \mathbf{A}\vec{x}_t + \vec{b} \rightarrow$$

$$\begin{Bmatrix} \dot{\theta}_t \\ \dot{w}_t \\ \ddot{\theta}_t \\ \ddot{w}_t \end{Bmatrix} = \begin{bmatrix} 0 & 0 & 1 & 0 \\ 0 & 0 & 0 & 1 \\ -\frac{k_\theta}{I_{2D}} & 0 & 0 & 0 \\ 0 & -\frac{k_w}{m_{2D}} & 0 & 0 \end{bmatrix} \begin{Bmatrix} \Delta\theta_t \\ \Delta w_t \\ \dot{\theta}_t \\ \dot{w}_t \end{Bmatrix} + \begin{Bmatrix} 0 \\ 0 \\ \frac{\rho_\infty v_\infty^2 c^2 c_m}{2 I_{2D}} \\ \frac{\rho_\infty v_\infty^2 c\, c_l}{2 m_{2D}} \end{Bmatrix}$$

$$(10)$$

4.3.2. 4$^{\text{th}}$ order Runge-Kutta

In the initial time steps of the calculation, the aeroelastic system is linearly solved using Equations (11) and (12). In these equations, $\mathbf{A}$ is the coefficient matrix and $\vec{b}$ the independent terms
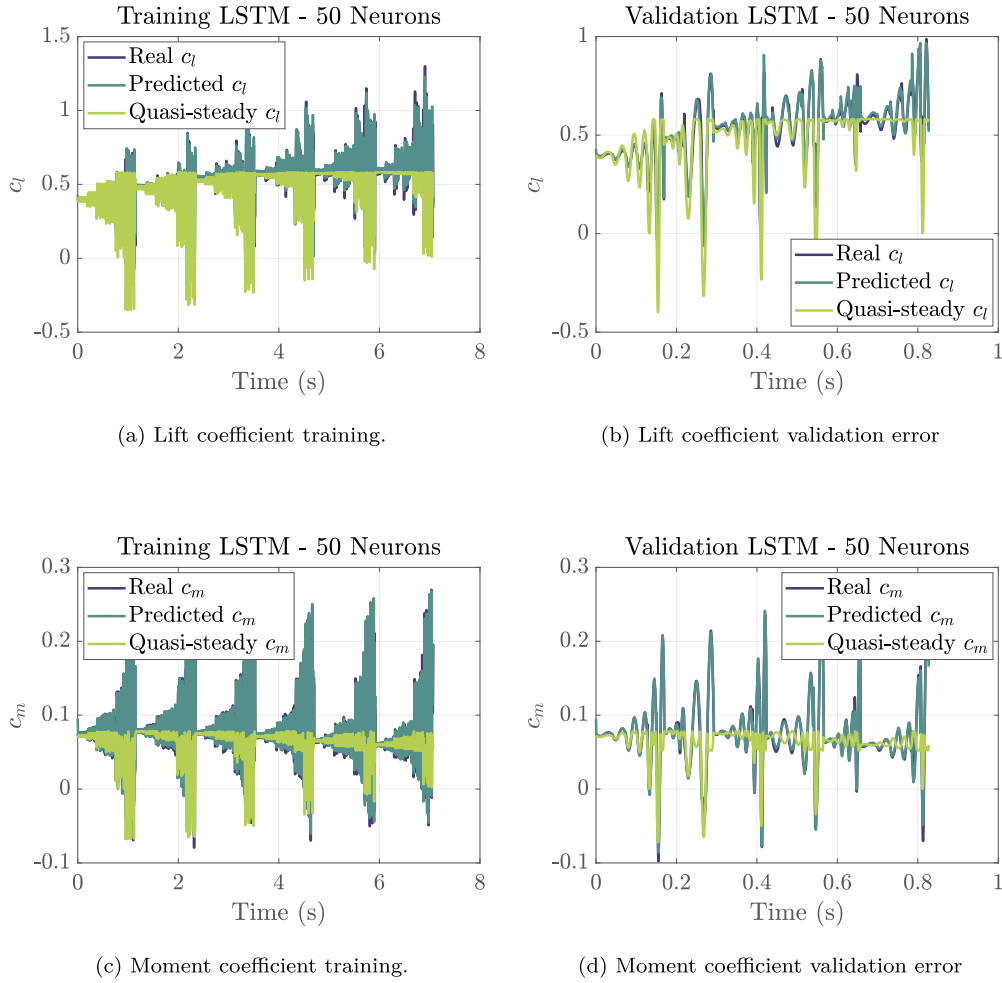
(a) Lift coefficient training.

(b) Lift coefficient validation error

(c) Moment coefficient training.

(d) Moment coefficient validation error

Fig. 13. Training and validation of the LSTM neural network.

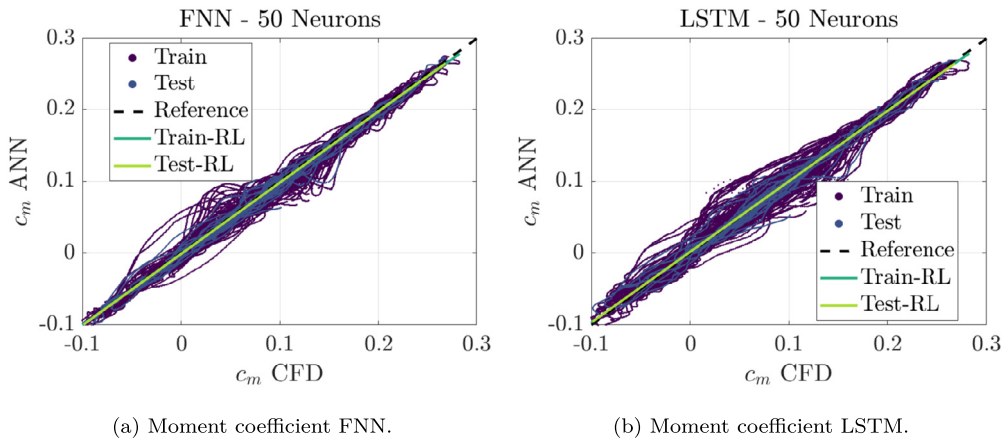(a) Moment coefficient FNN.

(b) Moment coefficient LSTM.

Fig. 14. Regression plots for the moment coefficient.

vector. The vectors $\vec{x}_t$ are the solution (pitch and plunge) of the problem.

$$\vec{f}_1 = \mathbf{A}\vec{x}_t + \vec{b} \qquad \vec{f}_2 = \mathbf{A}\left(\vec{x}_t + \tfrac{1}{2}\vec{f}_1 \Delta t\right) + \vec{b}$$

$$\vec{f}_3 = \mathbf{A}\left(\vec{x}_t + \tfrac{1}{2}\vec{f}_2 \Delta t\right) + \vec{b} \qquad \vec{f}_4 = \mathbf{A}\left(\vec{x}_t + \vec{f}_3 \Delta t\right) + \vec{b} \tag{11}$$

$$\vec{x}_{t+1} = \vec{x}_t + \frac{1}{6}\left(\vec{f}_1 + 2\vec{f}_2 + 2\vec{f}_3 + \vec{f}_4\right)\Delta t \tag{12}$$

4.3.3. 4 steps predictor-corrector

Each time step, the aeroelastic system is linearly solved using a 4 steps predictor-corrector method. This solver calculates the solution in a certain time step from the solution in the previous 4 time steps. Thus, it requires three steps of initialization using another algorithm, as 4th order Runge-Kutta. Using the same nomenclature than in 4.3.2, the numerical solver is presented in equations (13), (14) and (15).
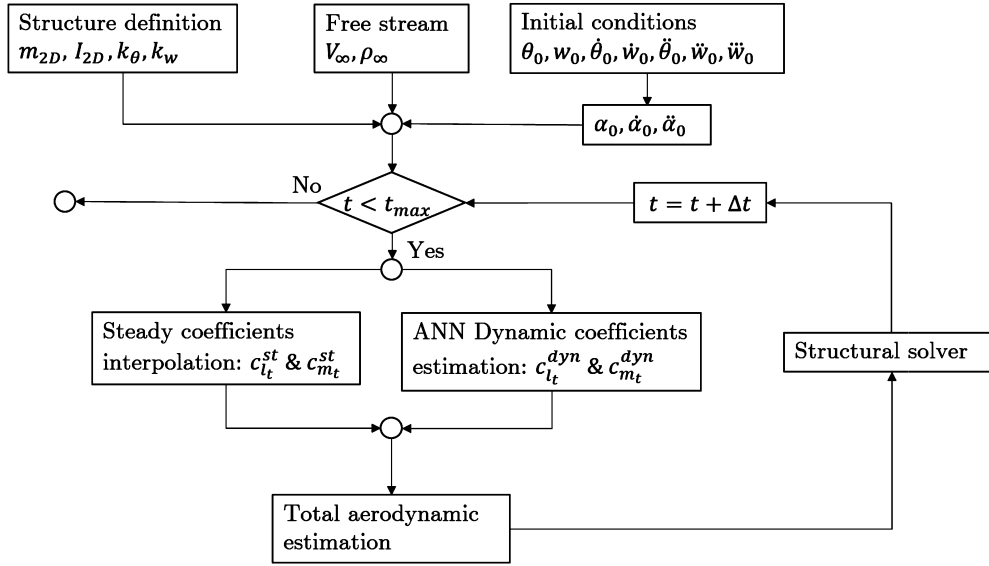
Fig. 15. Aeroelastic Reduced Order Model flow diagram.

(a) Stationary pitch moment coefficient
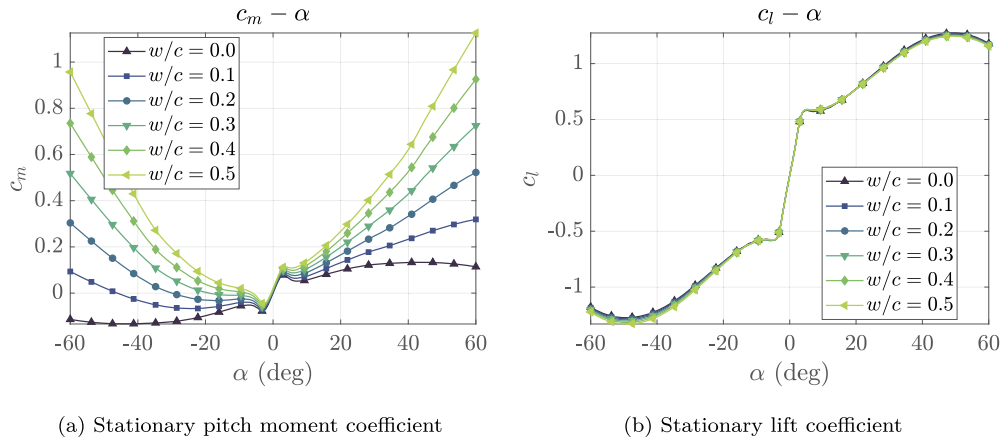
(b) Stationary lift coefficient

Fig. 16. Stationary aerodynamic coefficients as a function of the angle of attack and the plunge of the plate.

$$\vec{f} = \mathbf{A}\vec{x}_t + \vec{b} \tag{13}$$

$$\vec{x}_{pred} = \vec{x}_t + \frac{\Delta t}{24}\left(55\vec{f}\left(\vec{x}_t, \mathbf{A}, \vec{b}\right) - 59\vec{f}\left(\vec{x}_{t-1}, \mathbf{A}, \vec{b}\right)\right.$$
$$\left. + 37\vec{f}\left(\vec{x}_{t-2}, \mathbf{A}, \vec{b}\right) - 9\vec{f}\left(\vec{x}_{t-3}, \mathbf{A}, \vec{b}\right)\right) \tag{14}$$

$$\vec{x}_{t+1} = \vec{x}_t + \frac{1}{720}\left(251\vec{f}\left(\vec{x}_{pred}, \mathbf{A}, \vec{b}\right) + 646\vec{f}\left(\vec{x}_t, \mathbf{A}, \vec{b}\right)\right.$$
$$\left. - 264\vec{f}\left(\vec{x}_{t-1}, \mathbf{A}, \vec{b}\right) + 106\vec{f}\left(\vec{x}_{t-2}, \mathbf{A}, \vec{b}\right) - 19\vec{f}\left(\vec{x}_{t-3}, \mathbf{A}, \vec{b}\right)\right) \tag{15}$$

5. Results

5.1. CFD

The oscillating motion of the plate produces cycles which modify the value of the linear aerodynamic derivatives (Equation (16)). As mentioned in Section 3, the aerodynamic coefficients might be expressed as the sum of the stationary and the dynamic terms.

$$c_l = c_{l0} + c_{l\alpha}\alpha + c_{l\dot{\alpha}}\frac{c\dot{\alpha}}{V_\infty} + c_{l\ddot{\alpha}}\frac{c^2\ddot{\alpha}}{V_\infty^2} + \dots \tag{16}$$

As the section aerodynamics is nonlinear, CFD has been used for the calculation of the aerodynamic coefficients. In this section,

the stationary coefficient interpolation curves and the forced oscillation results are shown.

On one hand, in Fig. 16, the stationary coefficients are shown as a function of the angle of attack and the plunge. The coefficients exhibit a nonlinear behavior for angles of attack higher than 4 deg. In addition, the moment is significantly affected by the vertical position of the plate.

On the other hand, Fig. 17 shows the cyclic behavior of the aerodynamic coefficients due to the forced oscillation motion. Aerodynamic loops vary as a function of the initial angle of attack of the plate, the amplitude and the frequency of the movement. For low angles of attack, in the linear aerodynamic range (Figs. 17a and 17b), coefficient $c_{l\alpha}$ decreases with the frequency. In addition, the second derivative becomes higher, increasing the curvature of the loop. For post-stall conditions (Figs. 17c and 17d) the behavior of the system is highly nonlinear. In these cases, the effects of nonlinearities tend to increase with frequency. Thus, the coefficient presents an oscillating cycle with the frequency of the vortex shedding. In addition, for high initial incidences of the plate, an increase of the lift slope is noticed as an effect of the nonlinearities. The coefficient $c_{l\alpha}$ grows for the highest angles of attack becoming higher than the potential lift slope of 2π, as shown in Fig. 17c.

Legend: $f = 25\,\mathrm{Hz}$ $f = 45\,\mathrm{Hz}$ $f = 65\,\mathrm{Hz}$

$f\,(\mathrm{Hz})$	25	45	65
c_{l0}	0.40	0.40	0.40
$c_{l\alpha}$	4.84	3.00	1.75
$c_{l\dot\alpha}$	−2.47	0.27	1.77
$c_{l\ddot\alpha}$	−0.49	0.05	0.35

$f\,(\mathrm{Hz})$	25	45	65
c_{l0}	0.38	0.34	0.31
$c_{l\alpha}$	5.05	3.75	3.72
$c_{l\dot\alpha}$	−1.70	0.83	1.64
$c_{l\ddot\alpha}$	−0.34	0.17	0.33

(a) $\Theta = 0.3$ deg & $\theta_0 = 2.5$ deg.   (b) $\Theta = 5$ deg & $\theta_0 = 2.5$ deg.

$f\,(\mathrm{Hz})$	25	45	65
c_{l0}	0.58	0.59	0.60
$c_{l\alpha}$	12.56	4.35	−0.22
$c_{l\dot\alpha}$	−3.54	−3.46	−1.42
$c_{l\ddot\alpha}$	−0.71	−0.69	−0.28

$f\,(\mathrm{Hz})$	25	45	65
c_{l0}	0.70	0.68	0.57
$c_{l\alpha}$	6.36	3.13	3.88
$c_{l\dot\alpha}$	−3.71	0.10	1.51
$c_{l\ddot\alpha}$	−0.74	0.02	0.30

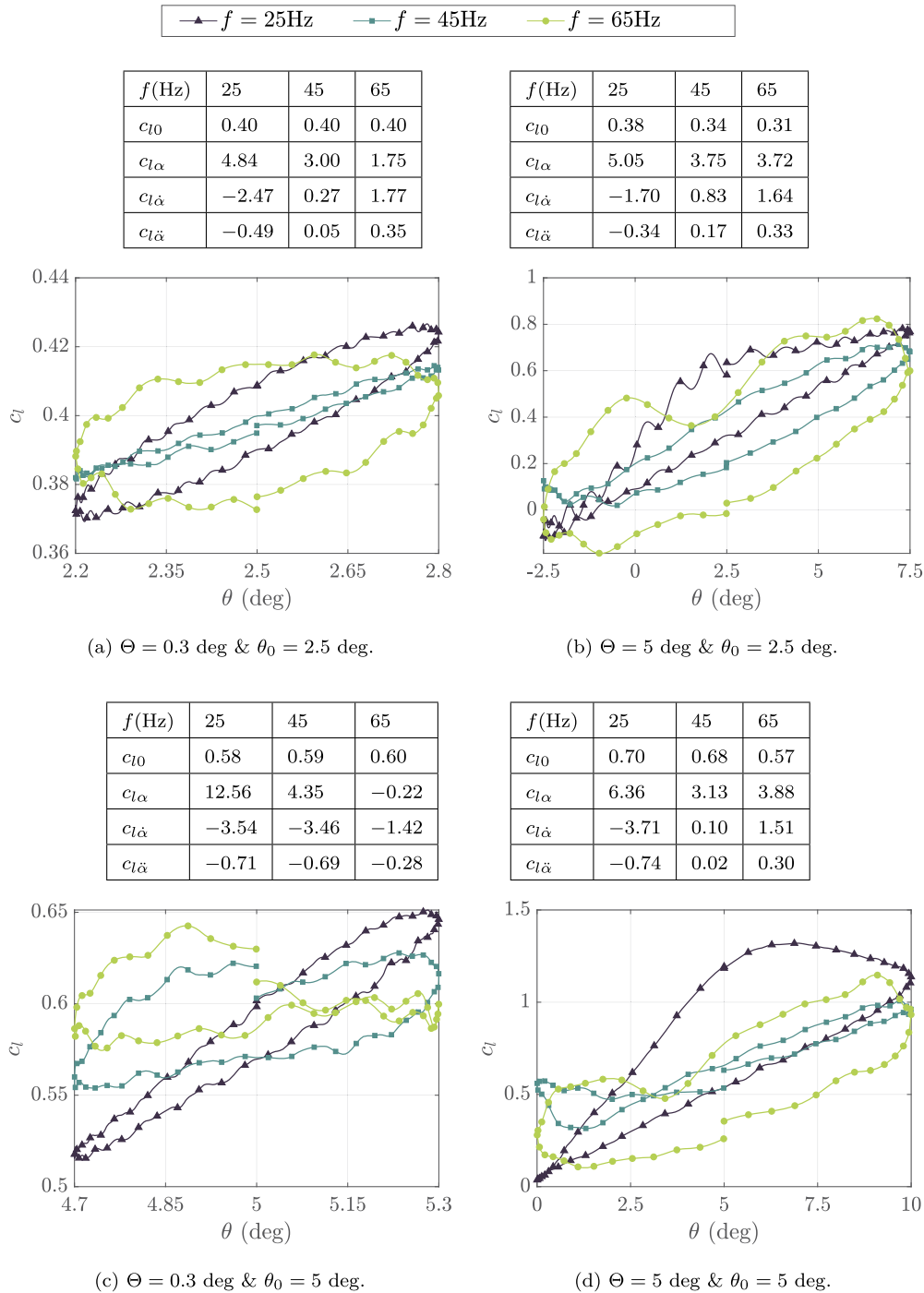(c) $\Theta = 0.3$ deg & $\theta_0 = 5$ deg.   (d) $\Theta = 5$ deg & $\theta_0 = 5$ deg.

Fig. 17. Aerodynamic cycles for a characteristic point of the dataset.

5.2. Aeroelastic ROM

The ROM is then tested on the equivalent rigid cross section of Fig. 1a. The nondimensional stiffness, k^*, is varied in order to represent different working conditions: stability range, limit cycle oscillation (LCO) and postflutter.

The ROM shows good accuracy to predict mean values of the deformation, as can be observed in Fig. 18. As stated in the previous sections, the utilization of artificial neural networks improves in a significant way the prediction of oscillatory nonlinear aerodynamics with respect to the steady polar, as it captures the dynamic effects on the flow which can damp the oscillation or prevent stall.

In addition, in Fig. 18 the instability zone may be identified as the characteristic stiffness in which there is an abrupt change in slope. The instability zone is represented by a shaded area. Inside this area the motion of the plate is amplified with time. The prediction of LCO and instabilities are also accurate with the use artificial neural networks. To evaluate the LCO prediction and the limitations of the ROM transient results, the amplitude and frequency of the predicted motion are analyzed.

Fig. 19 shows the amplitude of the simulated motion. Both FNN and LSTM show a fair similitude with the CFD simulation, while quasi-steady aerodynamics tend to overpredict the value of deformation for higher values of k^*. The stall flutter may be identified as the point where amplitude abruptly increases. The instability
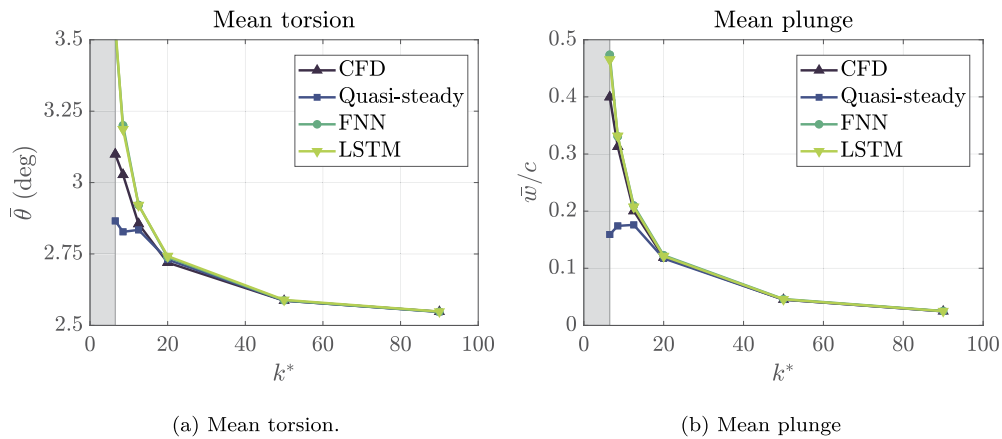
(a) Mean torsion.

(b) Mean plunge

Fig. 18. Comparison of the mean deformation of the ROM and CFD simulation for the different aerodynamic models.
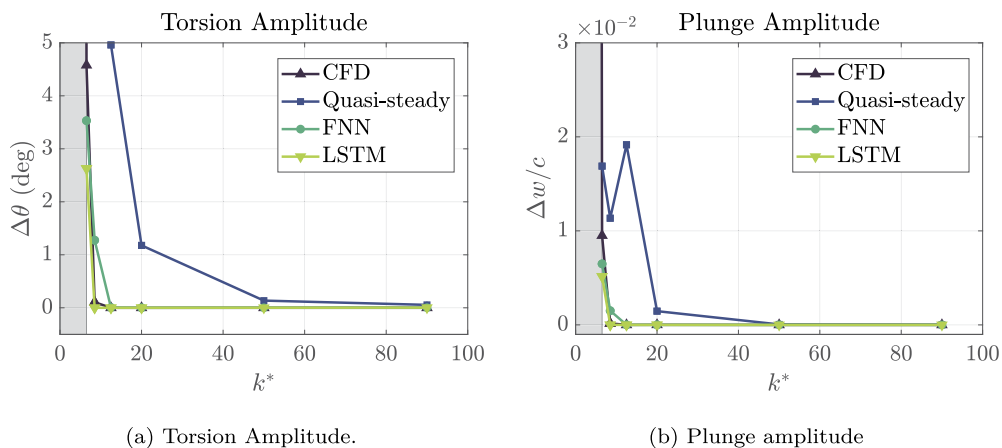

(a) Torsion Amplitude.

(b) Plunge amplitude

Fig. 19. Comparison of the amplitude of the motion of the ROM and CFD simulation using different aerodynamic models.

(a) Torsion cyclic evolution.
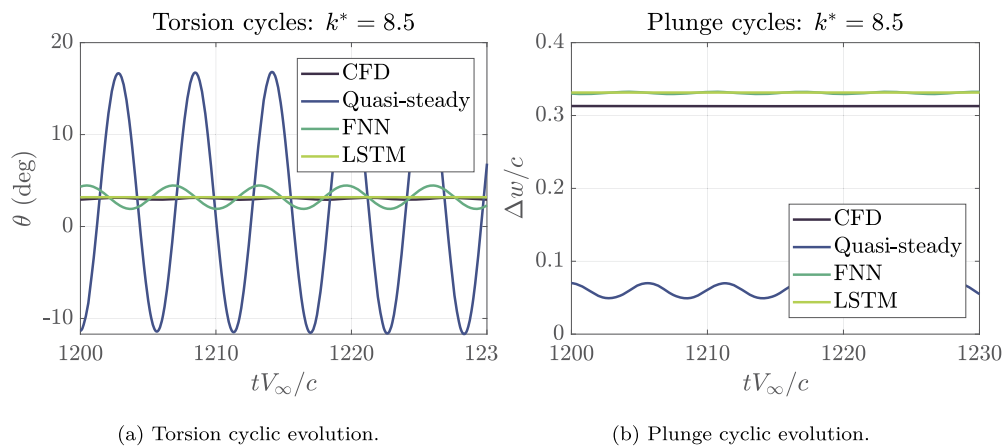
(b) Plunge cyclic evolution.

Fig. 20. Time cycles of torsion and plunge for a nondimesional stiffness of $k^* = 8.5$.

appears when the nondimensional stiffness decreases to the flut-ter value k_f^*, in other words, when the free velocity reaches the flutter velocity V_f.

However, although both typologies of neural networks show similar behaviors, slightly different results might be observed in the amplitude of the motion. FNN is more sensitive to the changes of stiffness. Therefore, before the stall flutter, the amplitude starts to increase. However, LSTM increases the aerodynamic damping. The motion is totally damped and only grows when it reaches the stall flutter condition. CFD aeroelastic simulation presents an intermediate situation. The motion starts to increase the ampli-tude in the same conditions than the FNN. Nevertheless, it is con-strained to low values, near to the damped aerodynamics, similarly to the LSTM (Fig. 20). In addition, when the stall flutter is reached, the CFD simulations increase the amplitude faster than the ANNs, Fig. 21.

Figs. 20 and 21 show the time evolution of the previous model for two different working conditions. In these figures, small differ-ences in the frequency of the oscillation may be observed. The fre-quency of the motion is also analyzed in Fig. 22, observing an error
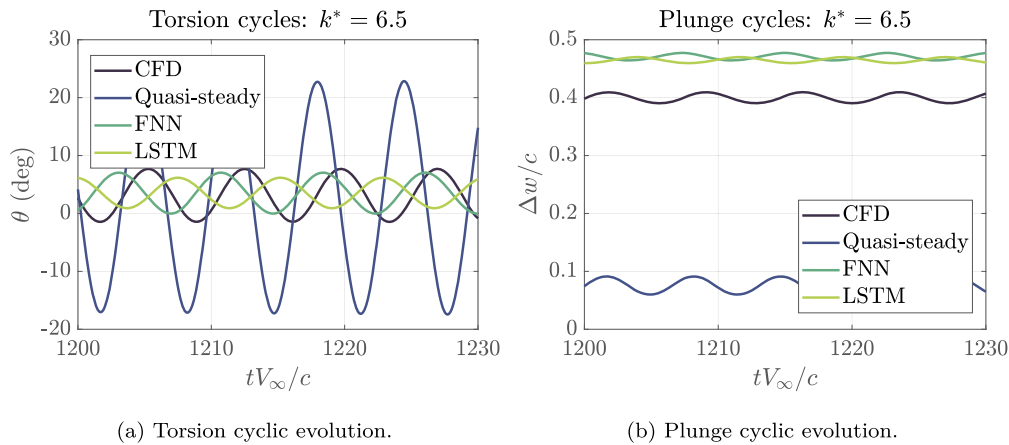
(a) Torsion cyclic evolution.

(b) Plunge cyclic evolution.

Fig. 21. Time cycles of torsion and plunge for a nondimesional stiffness of $k^* = 6.5$.

(a) Torsion frequency.
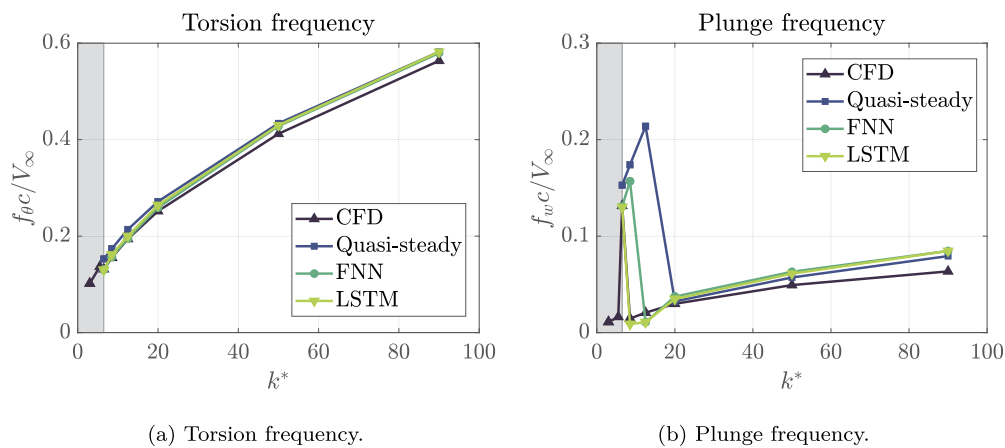
(b) Plunge frequency.

Fig. 22. Comparison of the frequency of the motion of the ROM and CFD simulation for the different aerodynamic models.

lower than 5% for the twist frequency. Differences in frequency are slightly more noticeable when analyzing plunge non-dimensional frequency, where they are of approximately 10% for nondimensional stiffness far from the aeroelastic instability. However, as it was observed at Figs. 18 and 19, the influence of this frequency is of second order when estimating nonlinear aeroelastic instabilities.

Finally, it is important to compare computational cost of the different models performed during this work. Note that all the simulations were performed on an Intel® Xeon® CPU ES-2630 v2, using 5 parallel processes. As an example, the average time for computing each simulation was of 10 hours for the CFD computations, and between 3 and 5 minutes for FNN and LSTM, respectively.

6. Conclusions

In this article, a Reduce Order Model (ROM), with a surrogate aerodynamic model based on Artificial Neural Networks (ANN), is developed for calculating an aeroelastic equivalent cross section. The main objective pursued is to test the accuracy of the ROM in the prediction of dynamic instabilities, as stall flutter, in nonlinear aerodynamic problems.

A flat plate is chosen as the studied geometry due to its nonlinear behavior. The aerodynamic coefficients of the plate are proved to vary with respect to the initial angle of attack, the amplitude and the frequency of the motion. In order to reproduce the different aerodynamic conditions that may appear around the plate, a set of CFD simulations have been calculated as the training dataset of the network. Nevertheless, the methodology and the test case

are prepared to be capable of using wind tunnel data. The ANN have been trained to reduce both training and validation errors and have been proved to be independent of the number of neurons. Two different typologies of network (FNN and LSTM), which are utilized for similar problems in the literature, are tested to compare the deformation obtained and the accuracy of the ROM.

The networks have been tested for different conditions, showing high accuracy to reproduce the aerodynamic coefficients of the cross section given its motion as input. Although there is a gain of accuracy comparing with the nonlinear steady polar, some effects are lost with the use of the surrogate model. For instance, the variations of the aerodynamic coefficients due to the fluctuations of the wake are not reproduced by the model. In addition, the ANNs tend to reproduce a sinusoidal oscillation of the coefficients, losing other effects as vortex shedding, which limits the range of application of the artificial neural networks. Thus, the procedure works for nonlinear aerodynamics, in a certain range of application in which the oscillations due to turbulence are small or negligible. For an oscillating plate, it may be applied for low angles of attack (approximately between -6 and 6 deg), low amplitudes of the oscillation (between 0 and 5 deg) and low or moderate frequencies (approximately a maximum of $\frac{fc}{V_\infty} = 0.3$). For higher frequencies the vortex shedding generated becomes more important and can reduce in a significant way the accuracy of the network.

The validation of the ANN shows that there is not a significant difference between the feed-forward neural network and the long short term memory network. The previous fact, added to the easier definition and training of the feed forward neurons, make this

typology more efficient to obtain the aerodynamic coefficients of a plate under low or moderate angles of attack.

Finally the ANNs have been coupled to a simplified structural solver. The results show an accurate prediction of the mean deformation in both torsion and plunge. The instability is also predicted accurately from the mean deformation curve as the point in which the slope of the curve increases abruptly. The time solutions have also been compared observing differences of behavior between the types of aerodynamic models. Quasi-steady aerodynamics shows a lack of accuracy when predicting a dynamic phenomenon. Both ANNs present similar results. However, the LSTM solution tends to damp the oscillation more than the CFD while FNN increases the amplitude and predicts the instability for a slightly lower free stream velocities.

As a summary, the previous facts lead to the following main conclusions:

- The aerodynamic loads in a dynamic problem are strongly conditioned by the mean angle of attack, the amplitude and the frequency of the oscillation. Thus, the stationary polar cannot be used to obtain accurate solutions.
- The utilization of artificial neural networks (ANN) may reduce both the time of simulation (compared with CFD simulations) and the error (compared with linear or steady models) in aeroelastic nonlinear problems.
- Different typologies of neural networks can be applied with similar results. However, recursive structures, for instance LSTM networks with the previous dataset and activation functions tend to damp the oscillation. On the other hand, FNN are faster and reduce the calculation cost, but they can be too conservative in the prediction of the aeroelastic instability.

Finally, this work completes the research developed in the literature, showing the applicability of the ANN to the aeroelastic problem, comparing different types of ANN and coupling the aerodynamics with the structure of the section. This procedure has been demonstrated to reduce in a significant way the computational cost and to preserve the accuracy of the solution for arbitrary sections and nonlinear aerodynamics.

Declaration of competing interest

The authors declare that they have no known competing financial interests or personal relationships that could have appeared to influence the work reported in this paper.

Acknowledgements

References

[1] G. Rogers, J. Kristof, Reducing operational and product costs through environmental accounting, Environ. Qual. Manag. 12 (2003) 17–42.

[2] S. Guo, Aeroelastic optimization of an aerobatic aircraft wing structure, Aerosp. Sci. Technol. 11 (2007) 396–404.

[3] C. Ledermann, P. Ermanni, R. Kelm, Dynamic cad objects for structural optimization in preliminary aircraft design, Aerosp. Sci. Technol. 10 (2006) 601–610.

[4] B. Briseghella, L. Fenu, C. Lan, E. Mazzarolo, T. Zordan, Application of topological optimization to bridge design, J. Bridge Eng. 18 (2013) 790–800.

[5] D.K. Koli, G. Agnihotri, R. Purohit, Advanced aluminium matrix composites: the critical need of automotive and aerospace engineering fields, Mater. Today 2 (2015) 3032–3041.

[6] M. Blair, T.A. Weisshaar, Swept composite wing aeroelastic divergence experiments, J. Aircr. 19 (1982) 1019–1024.

[7] L. Librescu, S. Thangjitham, Analytical studies on static aeroelastic behavior of forward-swept composite wing structures, J. Aircr. 28 (1991) 151–157.

[8] J.P. Thomas, E.H. Dowell, K.C. Hall, Nonlinear inviscid aerodynamic effects on transonic divergence, flutter, and limit-cycle oscillations, AIAA J. 40 (2002) 638–646.

[9] L. Sanches, T.A. Guimaraes, F.D. Marques, Aeroelastic tailoring of nonlinear typical section using the method of multiple scales to predict post-flutter stable lcos, Aerosp. Sci. Technol. 90 (2019) 157–168.

[10] A.S. Thelen, L.T. Leifsson, P.S. Beran, Multifidelity flutter prediction using local corrections to the generalized aic, Aerosp. Sci. Technol. 106 (2020) 106032.

[11] T. Zhou, E. Dowell, S.S. Feng, Computational investigation of wind tunnel wall effects on buffeting flow and lock-in for an airfoil at high angle of attack, Aerosp. Sci. Technol. 95 (2019) 105492.

[12] R. Camussi, A. Di Marco, C. Stoica, M. Bernardini, F. Stella, F. De Gregorio, D. Barbagallo, Wind tunnel measurements of the surface pressure fluctuations on the new vega-c space launcher, Aerosp. Sci. Technol. 99 (2020) 105772.

[13] M. Nikbay, P. Acar, Integrating analytical aeroelastic instability analysis into design optimization of aircraft wing structures, J. Appl. Eng. Math. 1 (2011) 237–253.

[14] F. Roizner, M. Karpel, Parametric flutter margin method for aeroservoelastic stability analysis, AIAA J. 56 (3) (2018) 1011–1022.

[15] J. Sodja, F. Roizner, R. De Breuker, M. Karpel, Experimental characterisation of flutter and divergence of 2d wing section with stabilised response, Aerosp. Sci. Technol. 78 (2018) 542–552.

[16] S. Evans, D. Bradney, P. Clausen, Development and experimental verification of a 5 kw small wind turbine aeroelastic model, J. Wind Eng. Ind. Aerodyn. 181 (2018) 104–111.

[17] T. Argentini, D. Rocchi, C. Somaschini, Effect of the low-frequency turbulence on the aeroelastic response of a long-span bridge in wind tunnel, J. Wind Eng. Ind. Aerodyn. 197 (2020) 104072.

[18] K. Fujii, Progress and future prospects of cfd in aerospace - wind tunnel and beyond, Prog. Aerosp. Sci. 41 (2005) 455–470.

[19] X. Dong, Y. Zhang, Y. Zhang, Z. Zhang, X. Lu, Numerical simulations of flutter mechanism for high-speed wide-chord transonic fan, Aerosp. Sci. Technol. 105 (2020) 106009.

[20] J. Ren, H. Huang, D. Wang, X. Dong, B. Cao, An efficient coupled-mode flutter analysis method for turbomachinery, Aerosp. Sci. Technol. 106 (2020) 106215.

[21] L. Wang, R. Quant, A. Kolios, Fluid structure interaction modelling of horizontal-axis wind turbine blades based on cfd and fea, J. Wind Eng. Ind. Aerodyn. 158 (2016) 11–25.

[22] C. Peng, H. Jinglong, Prediction of flutter characteristics for a transport wing with wingtip device, Aerosp. Sci. Technol. 23 (2012) 461–468.

[23] N. Tsushima, W. Su, Flutter suppression for highly flexible wings using passive and active piezoelectric effects, Aerosp. Sci. Technol. 65 (2017) 78–89.

[24] M. Amoozgar, S. Fazelzadh, H.H. Khodaparast, M. Friswell, J. Cooper, Aeroelastic stability analysis of aircraft wings with initial curvature, Aerosp. Sci. Technol. 107 (2020) 106241.

[25] H.J. Kwon, D.H. Kim, I. Lee, Frequency and time domain flutter computations of a wing with oscillating control surface including shock interference effects, Aerosp. Sci. Technol. 8 (2004) 519–532.

[26] Y. You, D. Na, S.N. Jung, Improved rotor aeromechanics predictions using a fluid structure interaction approach, Aerosp. Sci. Technol. 73 (2018) 118–128.

[27] C. Baxevanou, P. Chaviaropoulos, S. Voutsinas, N. Vlachos, Evaluation study of a Navier-Stokes cfd aeroelastic model of wind turbine airfoils in classical flutter, J. Wind Eng. Ind. Aerodyn. 96 (2008) 1425–1443.

[28] E. Dowell, A Modern Course in Aeroelasticity, Springer, 2015.

[29] E. Camilo, F.D. Marques, J.L.F. Azevedo, Hopf bifurcation analysis of typical sections with structural nonlinearities in transonic flow, Aerosp. Sci. Technol. 30 (2013) 163–174.

[30] D. Li, A.D. Ronch, G. chen, Y. Li, Aeroelastic global structural optimization using an efficient cfd-based reduced order model, Aerosp. Sci. Technol. 94 (2019) 105354.

[31] J. Luo, Design optimization of the last stage of a 4.5-stage compressor using a pod-based hybrid model, Aerosp. Sci. Technol. 76 (2018) 303–314.

[32] G. Chen, D. Li, Q. Zhou, A.D. Ronch, Y. Li, Efficient aeroelastic reduced order model with global structural modifications, Aerosp. Sci. Technol. 76 (2018) 1–13.

[33] K. Ghorbanian, M. Gholamrezaei, An artificial neural network approach to compressor performance prediction, Appl. Energy 86 (2009) 1210–1221.

[34] J.M. Luján, H. Climent, L.M. García-Cuevas, A. Moratal, Volumetric efficiency modelling of internal combustion engines based on a novel adaptive learning algorithm of artificial neural networks, Appl. Therm. Eng. 123 (2017) 625–634.

[35] J.M. Alonso, F. Alvarruiz, J.M. Desantes, L. Hernández, V. Hernández, G. Moltó, Combining neural networks and genetic algorithms to predict and reduce diesel engine emissions, IEEE Trans. Evol. Comput. 11 (2007).

[36] J. Peng, C. Luo, Z. Han, Z. Hu, G. Han, Z. Jiang, Parameter-correlation study on shock-shock interaction using a machine learning method, Aerosp. Sci. Technol. 107 (2020) 106247.

[37] T. Wu, A. Kareem, Modeling hysteretic nonlinear behavior of bridge aerodynamics via cellular automata nested neural network, J. Wind Eng. Ind. Aerodyn. 99 (2011) 378–388.

[38] C.-H. Chen, J.-C. Wu, J.-H. Chen, Prediction of flutter derivatives by artificial neural networks, J. Wind Eng. Ind. Aerodyn. 96 (2008) 1926–1937.

[39] T. Abbas, I. Kavrakov, G. Morgenthal, T. Lahmer, Prediction of aeroelastic response of bridge decks using artificial neural networks, Comput. Struct. 231 (2020) 106198.

[40] T. Li, T. Wu, Z. Liu, Nonlinear unsteady bridge aerodynamics: reduced-order modeling based on deep lstm networks, J. Wind Eng. Ind. Aerodyn. 198 (2020) 104116.

[41] A. Gil, A. Tiseira, P. Quintero, A. Cremades, Prediction of the non-linear aeroelastic behavior of a cantilever flat plate and equivalent 2d model, Aerosp. Sci. Technol. 113 (2021) 106685.

[42] A. Torregrosa, A. Gil, P. Quintero, A. Ammirati, H. Denayer, W. Desmet, Prediction of flow induced vibration of a flat plate located after a bluff wall mounted obstacle, J. Wind Eng. Ind. Aerodyn. 190 (2019) 23–39.

[43] B. Kröse, P. van der Smagt, An Introduction to Neural Networks, University of Amsterdam, 1996.

[44] S. Pope, Turbulent Flows, Cambridge University Press, 2009.

[45] R. Gavasane, P. Pai, V. Kumar, Numerical simulation of pitching and plunging motion of flat plate using oversetmeshes, in: Symposium on Applied Aerodynamics and Design of Aerospace Vehicle (SAROD 2013), 2013.

[46] J. Morgado, R. Vizinho, M. Silvestre, J. Páscoa, Xfoil vs cfd performance predictions for high lift low Reynolds number airfoils, Aerosp. Sci. Technol. 75 (2016) 207–214.

[47] D. Wilcox, Multiscale model for turbulent flows, in: Proceedings of the 24th AIAA Aerospace Science Meeting, Vol. 24, 1986, pp. 1311–1320.

[48] M.J. Emes, F. Ghanadi, M. Arjomandi, R.M. Kelso, Investigation of peak wind loads on tandem heliostats in stow position, Renew. Energy 121 (2018) 548–558.

[49] P.M. Quintero, Characterization of fluid structure interaction mechanisms and its application to vibroacoustic phenomena, Ph.D. thesis, Universitat Politècnica de València, 2019.

[50] J. Weiss, J. Maruszewski, W. Smith, Implicit solution of preconditioned Navier-Stokes equations using algebraic multigrid, AIAA J. 37 (1999) 29–36.

[51] J. Weiss, W. Smith, Preconditioning applied to variable and constant density flows, AIAA J. 33 (1995) 2050–2057.

[52] V. Venkatakrishnan, On the convergence of limiters and convergence to steady state solutions, AIAA-93-0880, 1995.

[53] H. Hadzic, Development and application of finite volume method for the computation of flows around moving bodies on unstructure, overlapping grids, 2005.

[54] P. Roache, Verification and Validation in Computational Science and Engineering, Hermosa Publishers, 1998.

[55] A.A. Adeniyi, H.P. Morvan, K.A. Simmons, A transient cfd simulation of the flow in a test rig of an aeroengine bearing chamber, Heat Transf. 5C (2014).

[56] I.V. Tetko, D.J. Livingstone, A.I. Luik, Neural network studies 1. Comparison of overfitting and overtraining, J. Chem. Inf. Comput. Sci. 35 (1995) 826–833.

[57] S. Yadav, S. Shukla, Analysis of k-fold cross-validation over hold-out validation on colossal datasets for quality classification, in: 6th International Advanced Computing Conference, 2016.

[58] W. Zhang, Y. Jiang, Z. Ye, Two better loosely coupled solution algorithms of cfd based aeroelastic simulation, Eng. Appl. Comput. Fluid Mech. 1 (2007).